



1 **The Role of Chemical Boundary Conditions in Simulating Summer Ozone and
2 Cross-Boundary Transport over China**

3

4

5 Yunsong Du^{1,2}, Fumo Yang¹, Sijia Lou³, Baolei Lyu⁴, Ran Huang⁵, Guangming Shi¹,
6 Yongtao Hu⁶, Yan Jiang⁷, Nan Wang^{1*}

7

8

9

10 ¹College of carbon Neutrality Future Technology, Sichuan University, Chengdu 610065, China

11 ²Department of Environmental Science and Engineering, Sichuan University, Chengdu 610065,
12 China

13 ³School of Atmospheric Sciences, Nanjing University, Nanjing 210023, China

14 ⁴Huayun Sounding Meteorological Technology Co. Ltd., Beijing 100081, China

15 ⁵Hangzhou AiMa Technologies, Hangzhou, Zhejiang 311121, China

16 ⁶School of Civil and Environmental Engineering, Georgia Institute of Technology, Atlanta,
17 Georgia 30332, USA

18 ⁷Sichuan Eco-environment Monitoring Station, Chengdu 610091, China

19

20 ***Correspondence:** Nan WANG (nan.wang@scu.edu.cn)

21



22 **Key Points**

23 1. We systematically evaluated the impacts of chemical boundary conditions (static vs.
24 dynamic) on regional O₃ simulations over China.

25 2. Chemical boundary conditions strongly modulate O₃ simulations via cross-
26 boundary transport in both horizontal and vertical directions.

27 3. Synoptic circulation dynamically amplifies the impacts of chemical boundary
28 conditions on regional O₃ levels.

29
30



31 **Abstract**

32 Regional chemical transport models are vital for diagnosing and forecasting
33 tropospheric ozone (O_3) pollution. However, their accuracy is often limited by the
34 simplified treatment of chemical boundary conditions (CBCs). This study provides a
35 comprehensive evaluation of how different CBCs influence regional O_3 simulations
36 over China using the WRF–CMAQ model. Four CBCs scenarios were assessed: a static
37 BASE profile representing climatological conditions and three dynamic scenarios
38 derived from H-CMAQ, GEOS-Chem, and CESM2.2. Model results were validated
39 with surface networks, ozonesonde profiles, and satellite O_3 columns. The BASE
40 scenario underestimated the average maximum daily 8-hour O_3 (avg-O3MDA8) and its
41 90th percentile by -5.7% and -13.1% , respectively, while dynamic CBCs substantially
42 improved the accuracy. GEOS-Chem achieved the lowest bias (-0.3%) and highest
43 agreement (0.85 and 0.83) for avg-O3MDA8 and its 90th percentile. H-CMAQ
44 performed best in high-elevation northwestern regions, and CESM2.2 excelled in
45 southern and southwestern areas. Vertically, all CBCs reasonably matched observations
46 within the troposphere, but elevated lower-stratosphere biases were identified in BASE,
47 H-CMAQ, and CESM2.2. A case study contrasting cyclone-scavenging and post-trough
48 accumulation phases revealed that dynamic CBCs enhance cross-boundary transport
49 efficiency, raising O_3 by 10–20% over eastern China through combined continental and
50 stratospheric inflows. These results underscore the crucial role of synoptic circulation–
51 driven transboundary transport in shaping regional O_3 concentrations and demonstrate
52 the importance of realistic, time-varying CBCs for improving regional O_3 simulations,
53 air quality forecasting, and transboundary pollution management in China.

54

55 **Key words:** O_3 simulation; cross-boundary transport; chemical boundary condition;
56 chemical transport model

57



58 1 Introduction

59 Ozone (O_3) pollution is a critical environmental issue with profound implications for
60 air quality (Malley et al., 2017; Chiu et al., 2023). As a secondary pollutant,
61 tropospheric O_3 is mainly formed through photochemical reactions involving
62 precursors such as nitrogen oxides (NO_x) and volatile organic compounds (VOCs)
63 under sunlight. Elevated O_3 concentrations pose severe risks to public health,
64 contributing to respiratory diseases and premature mortality, while also damaging
65 ecosystems and suppressing agricultural productivity (WHO, 2016; Wang et al., 2017;
66 Zhang et al., 2019a). In addition, as a highly reactive oxidant, tropospheric O_3 regulates
67 the atmospheric lifetime of numerous reactive trace gases by governing their chemical
68 transformations (Jacob, 2003).

69 O_3 pollution is currently one of the most pressing environmental challenges faced
70 globally. In many Western countries, stringent air pollution controls implemented since
71 the last century have led to stabilization or even declines in O_3 concentrations (Monks
72 et al., 2015; Tarasick et al., 2019). Over the past decades, China have experienced
73 frequent high-ozone episodes, drawing increasing attention from both the scientific
74 community and policymakers. Even though, China has only more recently undertaken
75 aggressive air quality improvement measures, most notably through the Air Pollution
76 Prevention and Control Action Plan launched in 2012, which mandated substantial
77 reductions in nitrogen oxide emissions. Despite these efforts, O_3 concentrations in
78 China have not shown a sustained decline; instead, they have continued to rise in major
79 urban agglomerations such as the North China Plain and the Yangtze River Delta
80 (Zhang et al., 2019b; Lu et al., 2020; Wang et al., 2020; Wang et al., 2022). Nevertheless,
81 the formation and distribution of O_3 are governed by the interplay of precursor
82 emissions, meteorology, and transport processes. Variations in the magnitude and
83 composition of anthropogenic and natural NO_x and VOC emissions shape the chemical
84 regime for O_3 production and loss. Meteorological conditions (e.g., temperature, solar
85 radiation, humidity, boundary layer dynamics, and circulation patterns) further
86 modulate photochemical reaction rates, vertical mixing, and horizontal transport, while
87 surface characteristics and complex topography can influence local stagnation and
88 recirculation. Together with regional and transboundary transport, as well as inflow
89 from the free troposphere and occasional stratosphere–troposphere exchange, these
90 processes determine background O_3 levels and lead to strong spatial and seasonal
91 heterogeneity in O_3 pollution (Monks et al., 2015; Lu et al., 2018).Regional chemical
92 transport models (CTMs) are essential tools for predicting and diagnosing air pollution,
93 particularly photochemical O_3 pollution. Unlike global models, which emphasize large-
94 scale atmospheric processes at coarse spatial resolutions, regional models such as the
95 Community Multiscale Air Quality (CMAQ) and the Weather Research and Forecasting
96 model with Chemistry (WRF-Chem) resolve chemical and physical processes at finer
97 spatial and temporal scales (Byun and Schere, 2006; Grell et al., 2005). This capability
98 enables them to capture the complex interactions among local emissions, meteorology,
99 and topography that govern the formation, transport, and dispersion of O_3 and its
100 precursors. However, the reliability of CTM-based O_3 simulations ultimately depends
101 on the accuracy and consistency of the meteorological fields, emission inputs, and



102 chemical boundary conditions that define the model environment (Hogrefe et al., 2018;
103 Solazzo et al., 2012).

104 Over the past decade, CTMs have become central to air quality forecasting, scientific
105 research, environmental assessment and policy evaluation (Yahya et al., 2015; Bai et
106 al., 2018; Wang et al., 2021b; Gao et al., 2024). Their flexible domain configurations
107 allow targeted simulations over regions with intense emissions or complex terrain, such
108 as urban agglomerations and mountainous areas (Wang et al., 2019; Mao et al., 2022a;
109 Dou et al., 2024). Besides, incorporating high-resolution emission inventories and
110 region-specific meteorological inputs further enhances their accuracy. Numerous
111 applications have demonstrated their scientific and practical value: Zhang et al. (2019b)
112 used WRF-CMAQ to disentangle the relative roles of anthropogenic emissions and
113 meteorology in $PM_{2.5}$ variability, while Mao et al. (2022a) reproduced multi-pollutant
114 trends across China between 2013 and 2019, validating CMAQ's long-term
115 performance. Wang et al. (2024) applied CMAQ to assess regional O_3 responses during
116 heatwaves, highlighting the strong sensitivity of O_3 formation to both emissions and
117 meteorological drivers. Collectively, these applications underscore the indispensable
118 role of regional CTMs in advancing mechanistic understanding of air pollution and in
119 guiding effective clean-air strategies (Yahya et al., 2015; Lei et al., 2023; Dou et al.,
120 2024; Geng et al., 2024).

121 Building on this foundation, substantial efforts have focused on improving the
122 performance and reliability of regional CTMs. A major area of optimization lies in
123 chemical mechanisms: updated frameworks such as Carbon Bond 6 (CB6) and SAPRC-
124 11 enhance model fidelity in representing O_3 formation pathways and secondary organic
125 aerosol production under diverse atmospheric conditions (Yarwood et al., 2010; Carter
126 and Heo, 2013). Parallel improvements in meteorological simulations—through
127 techniques such as four-dimensional data assimilation (FDDA) in WRF and the
128 incorporation of high-resolution land-use datasets (e.g., MODIS, NLCD)—have
129 sharpened the representation of surface temperature, planetary boundary layer height,
130 and wind fields (Mallard et al., 2018; Campbell et al., 2019; Godowitch et al., 2015;
131 Wang et al., 2021a; Siewert and Kroszczynski, 2023). Meanwhile, advances in
132 anthropogenic and biogenic emission inventories, including the Multi-resolution
133 Emission Inventory for China (MEIC) and the U.S. National Emissions Inventory (NEI),
134 now provide finer spatial and temporal detail, capturing sector-specific variability and
135 reducing input uncertainty (Li et al., 2017a; Zheng et al., 2021; Foley et al., 2023; Geng
136 et al., 2024). Together, these continuous advancements have considerably strengthened
137 the capacity of regional CTMs to support both scientific inquiry and evidence-based
138 policy-making.

139 Despite substantial advances in regional chemical transport models (CTMs),
140 comparatively little attention has been devoted to chemical boundary conditions
141 (CBCs), even though they critically influence model accuracy. CBCs specify the
142 concentrations of air pollutants at the lateral and vertical boundaries of the simulation
143 domain, thereby constraining internal chemical evolution and pollutant transport
144 (Goldberg et al., 2015; Hogrefe et al., 2018). Accurate CBCs are essential for capturing
145 the impact of long-range pollutant transport and representing background



146 concentrations, both of which strongly shape regional air quality. For regional O_3 , these
147 boundary-driven background levels can modulate the effectiveness of local emission
148 controls, alter the chemical sensitivity regime, and partly determine the spatial gradients
149 between upwind and downwind areas. In regions strongly influenced by continental
150 outflow, stratosphere–troposphere exchange, or marine inflow, poorly specified CBCs
151 may therefore lead to systematic biases in simulated O_3 distributions (Zhu et al., 2024;
152 Goldberg et al., 2015; Hogrefe et al., 2018). Oversimplified treatments—such as
153 prescribing fixed background values or climatological means—can introduce
154 substantial biases, resulting in misrepresentation of pollutant levels and misleading
155 evaluations of source contributions, policy effectiveness, and health risks (Yahya et al.,
156 2015; Hogrefe et al., 2018). Indeed, sensitivity studies show that uncertainties in CBCs
157 can alter simulated O_3 by several parts per billion, with particularly pronounced effects
158 in downwind and coastal regions influenced by transboundary transport (Hogrefe et al.,
159 2018; Jerrett et al., 2005).

160 In China, few studies have systematically assessed the role of chemical boundary
161 conditions in influencing model performance or pollutant attribution across different
162 geographical regions (Zhu et al., 2024). This represents a critical gap, as the spatial
163 heterogeneity of transboundary influences—from continental transport in the west to
164 marine outflow in the east—could lead to regionally differentiated impacts on pollutant
165 concentrations and control policy outcomes. For example, western and northern China
166 may be more strongly affected by inflow of polluted air masses from upwind continental
167 source regions, while eastern coastal areas can be influenced by recirculation and clean
168 or polluted marine air, leading to distinct baseline O_3 levels and vertical structures.
169 Without an explicit assessment of CBCs across these contrasting regimes, regional
170 CTM applications may under- or overestimate O_3 burdens and misattribute observed
171 spatial patterns to local emissions or meteorology alone (Solazzo et al., 2012; Ni et al.,
172 2018; Sahu et al., 2021; Mao et al., 2022b; Shen et al., 2024). Therefore, a
173 comprehensive evaluation of the role of chemical boundary conditions in regional CTM
174 applications is urgently needed to enhance model reliability, reduce forecast uncertainty,
175 and support the formulation of more effective O_3 mitigation strategies.

176 Herein, we used outputs from three global chemical transport models to provide
177 downscaled CBCs for the regional CMAQ model and systematically evaluated the
178 impact of including versus omitting CBCs on O_3 simulations. Surface observations,
179 ozonesonde profiles, and satellite data were used to assess model performance across
180 China. We also examine the mechanisms by which CBCs influence O_3 , including their
181 regulation of background concentrations and propagation of transboundary pollutants
182 into the domain. This study advances understanding of CBCs in regional air quality
183 modeling and provides a foundation for more accurate high-resolution O_3 forecasts and
184 improved air quality management strategies. By explicitly contrasting simulations with
185 and without chemically consistent CBCs, while keeping emissions and meteorology
186 unchanged, this study isolates the contribution of boundary conditions from other key
187 drivers of O_3 variability. The resulting diagnostics provide a clearer physical
188 interpretation of how CBCs interact with regional emissions and meteorological fields
189 to shape O_3 distributions over China.



190 **2 Data and Method**

191 **2.1 Modelling Configuration**

192 In this study, O₃ concentrations during July–August 2019 were simulated using the
193 WRF-CMAQ modeling system. The Weather Research and Forecasting (WRF,
194 <https://www.mmm.ucar.edu/models/wrf>) model version 3.9.1 was used to generate
195 meteorological fields, which were then provided as inputs to drive the Community
196 Multiscale Air Quality (CMAQ) model version 5.3.3 (<http://www.epa.gov/cmaq>).
197 CMAQ solves the governing physical and chemical equations to simulate the three-
198 dimensional distribution of air pollutants. The simulations were conducted at a
199 horizontal resolution of 36 km, covering the entire Chinese mainland and surrounding
200 regions to ensure adequate representation of regional transport processes. (see Fig. 1).
201 The meteorological initial and boundary conditions were derived from the ERA5
202 reanalysis dataset (0.25° × 0.25° resolution), provided by the Copernicus Climate
203 Change Service via the Climate Data Store (CDS) (Hersbach et al., 2023) .
204 Anthropogenic emissions over China were obtained from the Multi-resolution Emission
205 Inventory for China (MEIC v1.4) for the year 2019 (Li et al., 2017a), which provides
206 sector-based emissions mapped to CMAQ species (<http://meicmodel.org>, last accessed:
207 January 1, 2024). For regions outside China, the MIX v1.1 inventory was used, which
208 is also developed by Tsinghua University (Qiang Zhang) with input from Asia Center
209 for Air Pollution Research (Jun-ichi Kurokawa and Toshimasa Ohara), Konkuk
210 University (Jung-Hun Woo), Argonne National Laboratory (Zifeng Lu and David
211 Streets), and Peking University (Yu Song) (Li et al., 2017b) and includes regionalized
212 emissions for East Asia. The biogenic emissions were estimated using the inline
213 Biogenic Emission Inventory System (BEIS3) embedded within CMAQ which
214 dynamically calculates emissions based on land use, vegetation type, and
215 meteorological conditions online. The gas-phase chemistry was represented using the
216 SAPRC07TC mechanism, while aerosol processes were simulated using the AERO6
217 module.

218 In order to assess the influence of CBCs on O₃, four different CBC scenarios were
219 designed and applied as inputs to the CMAQ BCON (boundary condition) module. The
220 first scenario, referred to as BASE, employs a spatially uniform and temporally constant
221 boundary condition derived from the built-in ASCII vertical profiles in CMAQ. These
222 profiles were extracted from a hemispheric CMAQv5.3 beta2 simulation for the year
223 2016, representing annual mean concentrations at the grid cell nearest to (37N, -157W),
224 which is over the ocean in the central North Pacific region. Therefore, the BASE CBCs
225 represent the background profile of the open ocean environment. In contrast, the
226 remaining three scenarios utilize boundary conditions generated from the output of
227 three global chemistry models (GCMs), namely, Hemisphere version of the Community
228 Multiscale Air Quality model (H-CMAQ), Goddard Earth Observing System-
229 Chemistry (GEOS-Chem), and Community Earth System Model version 2.2
230 (CESM2.2). Each of these boundary datasets was processed and formatted consistently
231 to ensure compatibility with the CMAQ framework.

232 Specifically, CBCs for the H-CMAQ scenario were derived from daily averaged species



233 concentration outputs produced by a hemispheric CMAQ simulation under the U.S.
234 EPA's Air Quality Time Series (EQUATES) Project
235 (<http://www.epa.gov/cmaq/EQUATES>, last accessed: 1 August 2024). These
236 simulations were conducted using a customized version of CMAQ v5.3.2, with a
237 horizontal resolution of 108×108 km on a polar stereographic projection, and
238 employed the CB6R3M_AE7_KMTBR chemical mechanism.
239 For the GEOS-Chem scenario, 3-hourly global simulation outputs were used. The
240 GEOS-Chem model is a global 3-D chemical transport model driven by meteorological
241 fields from NASA's Goddard Earth Observing System (GEOS), developed by the
242 NASA Global Modeling and Assimilation Office. The chemical mechanism includes
243 comprehensive tropospheric O_3 - NO_x -VOCs-aerosol-halogen chemistry (Mao et al.,
244 2013; Park et al., 2004; Parrella et al., 2012; Wang et al., 1998), as well as stratospheric
245 chemistry processes (Eastham et al., 2014). Further information is available at
246 <https://geoschem.github.io/> (last accessed: 1 August 2024).
247 The CESM2.2 scenario utilized 6-hourly output from the Community Atmosphere
248 Model with Chemistry (CAM-chem) embedded within the Community Earth System
249 Model version 2.2 (CESM2.2). The CAM-chem simulations used the finite-volume
250 dynamical core, with a horizontal resolution of $1^\circ \times 1^\circ$ and 32 vertical levels. The
251 MOZART-T1 mechanism was applied to simulate both tropospheric and stratospheric
252 chemical processes. Details on the model setup and outputs are available at
253 <https://www2.acom.ucar.edu/gcm/cam-chem>.
254 All the three global model outputs were converted to the I/O API format required by
255 the CMAQ Chemical Transport Model (CCTM). A combination of data transformation
256 tools and custom scripts was developed and applied to harmonize species mapping,
257 spatial resolution, temporal alignment, and file formatting, thus enabling seamless
258 integration of each global model dataset as boundary conditions for the regional CMAQ
259 simulations. To minimize the influence of initial conditions and allow the imposed
260 boundary conditions to fully propagate throughout the simulation domain, a 10-day
261 model spin-up period was applied prior to the analysis period.
262



263 **2.2 Observation data**

264 **2.2.1 Surface observation data**

265 Surface observations across China for July–August 2019 were used to evaluate the
266 simulated meteorological parameters and atmospheric pollutant concentrations from
267 the WRF-CMAQ model. Meteorological data were obtained from the National
268 Meteorological Information Center (<http://data.cma.cn>, last accessed 1 January 2024).
269 Hourly meteorological observations from 2,394 monitoring stations were collected,
270 including 2-meter air temperature (T2), 2-meter relative humidity (RH2), 10-meter
271 wind speed (WS10), and surface pressure (PRS). Hourly O₃ observations were retrieved
272 from the China National Environmental Monitoring Center
273 (<https://air.cnemc.cn:18007/>, last accessed 1 January 2024), encompassing data from
274 1,480 air quality monitoring sites. The spatial distribution of meteorological and air
275 quality monitoring stations is shown in Fig. 1 and Fig. S1. To investigate the spatial
276 variability of chemical boundary condition impacts on O₃ simulation, monitoring sites
277 were grouped into seven regions within China (Fig. 1 and Table S1): South (S), East
278 (E), North (N), Central (C), Northeast (NE), Northwest (NW), and Southwest (SW).
279 This study evaluates sites O₃ using the Maximum Daily 8-Hour Average concentration
280 (O3MDA8), derived from both surface observations and model simulations. To
281 comprehensively assess model performance across different pollution levels, we
282 analyze two key indicators: the average O3MDA8 (avg-O3MDA8), which reflects the
283 overall background and typical exposure level, and the 90th percentile of O3MDA8
284 (90th-O3MDA8), which is used to characterize high-O₃ events. The inclusion of the
285 90th percentile metric enables evaluation of the model's ability to capture peak O₃
286 pollution episodes that are most relevant to regulatory thresholds and public health risk
287 assessments.

288 Model performance was quantitatively evaluated using multiple statistical metrics,
289 including mean observed value (OBS), mean simulated value (SIM) for each of the four
290 CBC scenarios (BASE, H-CMAQ, GEOS-Chem, CESM2.2), mean bias (MB),
291 normalized mean bias (NMB), root mean square error (RMSE), index of agreement
292 (IOA), and Pearson correlation coefficient (r). The mathematical definitions of these
293 statistics are provided below.

294
$$OBS = \frac{1}{n} \sum_{i=1}^n O_i$$

295
$$SIM = \frac{1}{n} \sum_{i=1}^n S_i$$

296
$$MB = \frac{1}{n} \sum_{i=1}^n (S_i - O_i)$$

297
$$NMB = \frac{\sum_{i=1}^n (S_i - O_i)}{\sum_{i=1}^n O_i}$$



298

$$\text{RMSE} = \sqrt{\frac{1}{n} \sum_{i=1}^n (S_i - O_i)^2}$$

299

$$r = \frac{\sum_{i=1}^n (S_i - \text{SIM})(O_i - \text{OBS})}{\sqrt{\sum_{i=1}^n (S_i - \text{SIM})^2} \sqrt{\sum_{i=1}^n (O_i - \text{OBS})^2}}$$

300

$$\text{IOA} = 1 - \frac{n * \text{RMSE}^2}{\sum_{i=1}^n (|S_i - \text{OBS}| + |O_i - \text{OBS}|)^2}$$

301

where S_i and O_i are the simulated and observed site's avg-O3MDA8 or 90th-O3MDA8, n represents the number of the simulated days.

303

2.2.2 Vertical Observation Data

304

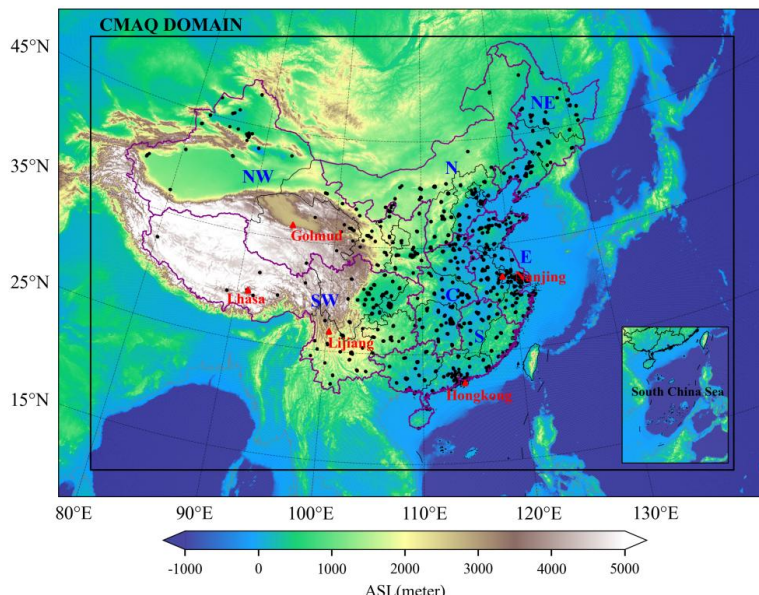
To evaluate the influence of CBCs on the vertical distribution of O_3 , O_3 sounding data from five representative sites (Hong Kong, Nanjing, Golmud, Lhasa, and Lijiang) were collected and used to validate the model's vertical O_3 simulations. These stations are strategically located in the eastern, southern, southwestern, and northwestern boundaries of the modeling domain (Fig 1), enabling a targeted assessment of how boundary conditions affect O_3 concentrations aloft. Briefly, the Hong Kong profiles (King's Park Observatory; launched at 13:00 LST; 9 soundings during July–August 2019) were obtained from the World Ozone and Ultraviolet Radiation Data Centre (WOUDC, <https://woudc.org/data.php>, last accessed: October 8, 2024). Nanjing observations (from the National Benchmark Climate Station; launched between 13:00 and 14:00 LST; 4 soundings between July 23, 2019 and September 1, 2020) were sourced from the China Air Pollution Data Center (CAPDC, <https://www.capdatabase.cn>, last accessed: October 8, 2024). Data for Golmud (12 profiles), Lhasa (8 profiles), and Lijiang (5 profiles), collected between 2019 and 2022 with launch times ranging from 23:00 to 02:00 LST, were obtained from the National Tibetan Plateau Data Center (TPDC, <https://data.tpdc.ac.cn/home>, last accessed: October 10, 2024) (Bai Zhixuan, 2023; Zhixuan, 2023; Bai Zhixuan, 2022). To ensure consistency across datasets and comparability with the model output, all sonde data were processed for the 0–20 km altitude range and interpolated to match the model vertical structure. Observations during July–August were prioritized, and model outputs were extracted as time-averaged vertical profiles over the corresponding grid cells and times (13:00 -14:00 or 23:00 - 2:00 LST). Detailed information about the surface observation and sounding sites is provided in Table S2.

327

In addition, tropospheric O_3 column data were also introduced to further evaluate the spatial performance of the model. This dataset was developed by the University of Science and Technology of China (USTC) and is derived from measurements by the Environmental Trace Gases Monitoring Instrument (EMI) aboard the Gaofen-5 satellite, China's first ultraviolet-visible hyperspectral spectrometer dedicated to atmospheric composition monitoring. The product provides a seamless tropospheric O_3 column dataset at a high spatial resolution of 1 km × 1 km, offering detailed information on O_3



334 distribution over complex terrains and urban regions. Further details on the retrieval
335 algorithm and validation of the product can be found in (Zhao et al., 2024). Detailed
336 information about the Tropospheric O₃ column data is also provided in Table S2.
337



338
339 **Figure 1.** Simulation domain of the CMAQ model with a horizontal resolution of 36 × 36 km. Black dots
340 represent surface O₃ monitoring sites, and red triangles denote O₃ sounding launch stations. Terrain
341 elevation above sea level (ASL) is illustrated with shaded relief. Purple lines delineate the administrative
342 boundaries of China's major regions—South (S), East (E), North (N), Central (C), Northeast (NE),
343 Northwest (NW), and Southwest (SW). The provinces included in each region are listed in Table S1.

344 **3. Results and Discussions**

345 **3.1 Comparative Analysis of four CBCs**

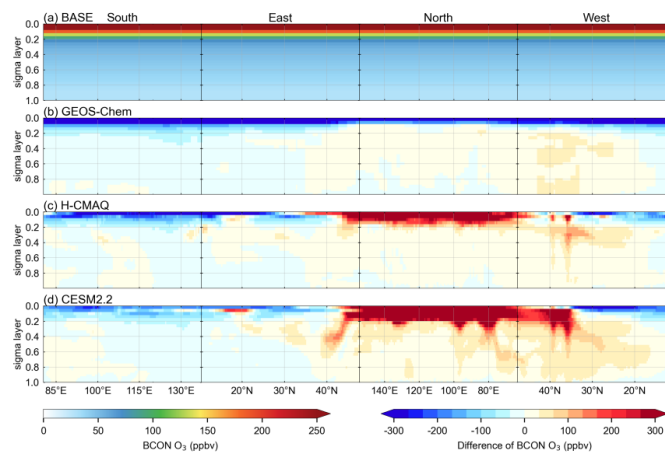
346 Fig. 2 displays the vertically averaged temporal O₃ distribution along the four lateral
347 boundaries of the modelling domain during July-August 2019, under four different
348 CBC scenarios. In the BASE scenario, the O₃ profile remains static, characterized by
349 horizontally uniform mixing ratios at each altitude. A sharp increase in O₃ concentration
350 is evident near the tropopause, with minimal vertical variation in the lower and mid-
351 troposphere. This relatively uniform, three-dimensional O₃ distribution suggests that
352 the BASE CBC scenario represents a background condition (i.e, over the open ocean),
353 and thus fails to adequately capture the spatiotemporal variability of O₃ over mainland
354 East Asia, where O₃ levels are strongly influenced by anthropogenic emissions and
355 regional transport processes.

356 In contrast to the static pattern in the BASE scenario, the O₃ boundary conditions
357 extracted from the three global models (H-CMAQ, GEOS-Chem, and CESM2.2)
358 exhibit both horizontal and vertical variability across the four lateral boundaries. These



359 three scenarios display a generally consistent spatial and vertical structure. However,
360 notable differences still exist across different boundaries. In the lower troposphere (0–
361 3 km), the average O_3 concentrations from the three global models are 5–7 ppbv lower
362 than those in the BASE scenario along the southern and eastern boundaries, with only
363 minor differences among the models. For instance, over the oceanic portions of these
364 boundaries, specifically the eastern segment of the southern boundary and the southern
365 segment of the eastern boundary, the BASE scenario overestimates boundary O_3
366 concentrations by as much as 20–30 ppbv. In contrast, along the northern and western
367 boundaries, the global models generally produce 4–20 ppbv higher O_3 concentrations
368 than the BASE scenario, accompanied by greater inter-model variability. Among them,
369 H-CMAQ and GEOS-Chem show relatively similar patterns, whereas CESM2.2
370 exhibits substantially higher O_3 levels, particularly along the western boundary (Fig. 2
371 and Table 1).

372 Conversely, compared to the BASE scenario, the differences in boundary O_3
373 concentrations among the three global models significantly increased in the mid-to-
374 upper troposphere (3–10 km) and stratosphere (above 10 km). In the mid-to-upper
375 troposphere (3–10 km), the BASE scenario generally underestimated O_3 concentrations
376 along the northern and western boundaries, while significantly overestimating them
377 along the southern boundary. The CESM2.2 scenario showed higher O_3 concentrations
378 along the eastern, northern, and western boundaries. In the stratosphere (above 10 km),
379 the global model results indicated that the BASE scenario significantly overestimated
380 O_3 concentrations along the southern, eastern, and western boundaries, with GEOS-
381 Chem exhibiting the lowest O_3 concentrations among the four scenarios. The H-CMAQ
382 and CESM2.2 models showed large areas of high O_3 concentration near the northern
383 boundary. These spatial variations in O_3 boundary conditions are likely to have a
384 considerable impact on the simulation of surface O_3 concentrations over China during
385 the summer months.



386
387 **Figure 2.** Temporally averaged O_3 chemical boundary conditions along the lateral boundaries of CMAQ
388 modeling domain. Panels show (a) BASE scenario O_3 concentrations, (b) GEOS-CHEM minus BASE ,
389 (c) H-CMAQ minus BASE, and (d), CESM2.2 minus BASE. Values are plotted clockwise, starting from
390 the southwest corner of the CMAQ simulation domain, with the model's sigma coordinates.



391 **Table 1.** Statistical results of average O₃ concentrations (ppbv) at various vertical heights among the
392 four boundaries for four CBC scenarios.

Vertical altitude	Boundary	BASE	H-CMAQ	GEOS-Chem	CESM2.2
0-3 km	South	31.7	27.3	25	26
	East	31.7	24.9	23.8	25.1
	North	31.7	39.5	36.4	47.4
	West	31.7	43.5	45.8	51.7
3-10 km	South	53.2	40.1	26.7	35.6
	East	53.2	54.9	43.4	61.7
	North	53.2	79.2	68.4	119.7
	West	53.2	76.2	60.6	88.7
Above 10 km	South	408.0	233.4	42.4	272.0
	East	408.0	351.6	82.0	373.8
	North	408.0	658.3	186.9	728.7
	West	408.0	338.6	88.2	324.1

393 **3.2 Evaluation of Model Performance Using Different CBCs**

394 **3.2.1 Meteorological simulation evaluation**

395 Table 2 presents an evaluation of WRF model simulations of 2-meter temperature (T2),
396 2-meter daily maximum temperature (T2max), 2-meter relative humidity (RH2), 10-
397 meter wind speed (WS10), surface pressure (PRS), and precipitation (PRECIP). The
398 data were averages from 2439 meteorological stations across China. Analysis of mean
399 bias (MB), correlation coefficient (r), and index of agreement (IOA) revealed that the
400 WRF model accurately simulated the meteorological fields. T2, T2max, RH2, and PRS
401 exhibited IOA values exceeding 0.85, indicating strong agreement with observations.
402 Correlation coefficients (r) exceeded 0.7 for all variables except WS10. However, some
403 biases remained in the simulation results for certain variables. Specifically, RH2 and
404 PRS were slightly underestimated, while PRECIP was overestimated; nevertheless, the
405 r and IOA values remained relatively high. In contrast, WS10 was significantly
406 overestimated (by 1.6 m/s), with both IOA and r below 0.5. This likely stemmed from the
407 relatively coarse model grid resolution, hindering accurate representation of urban
408 topography and its impact on wind speed—a phenomenon observed in other studies
409 (Hu et al., 2016; Shen et al., 2022). Overall, the WRF model demonstrated good
410 performance in meteorological simulations, providing reliable inputs for the CMAQ
411 model.

412
413



414

Table 2. Evaluation results for the meteorological variables.

variable	OBS	SIM	MB	RMSE	IOA	r
T2 (°C)	25	24.4	-0.6	2.1	0.94	0.91
T2max (°C)	29.9	29.3	-0.6	2.5	0.91	0.86
RH2 (%)	73.6	69.1	-4.5	8.6	0.88	0.86
WS10 (m/s)	2	3.6	1.6	1.8	0.41	0.45
PRS (hPa)	937.8	922.7	-15.1	28.5	0.97	0.97
PRECIP (mm)	297.4	434.3	136.9	234.2	0.72	0.7

415 3.2.2 Surface O₃ Simulation Performance

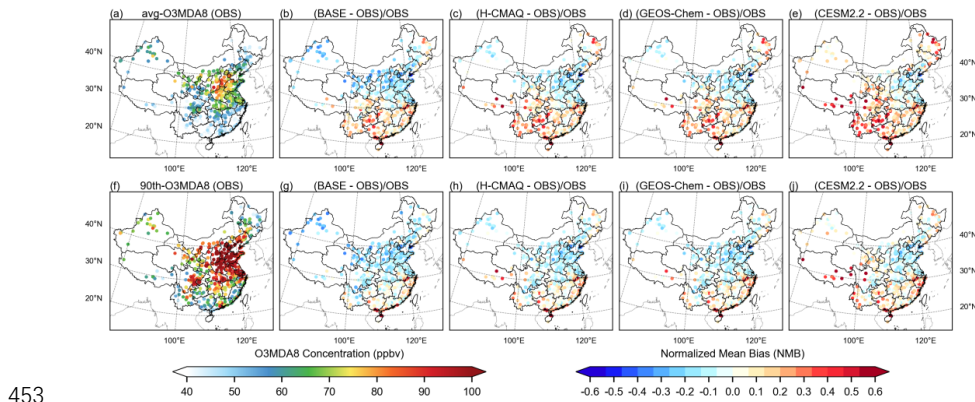
416 Fig. 3 illustrated the spatial distribution of avg-O3MDA8 and 90th-O3MDA8
 417 concentrations and their normalized mean bias (NMB) across China. Across all
 418 monitoring sites, the observed avg-O3MDA8 and 90th-O3MDA8 for July-August 2019
 419 were 59.4 ppbv and 82.8 ppbv, respectively (Table S3). Generally, O₃ concentrations in
 420 North China were higher than in South China. For 90th-O3MDA8, elevated values were
 421 widespread, notably in the North China Plain (NCP), Central China, Yangtze River
 422 Delta (YRD), Pearl River Delta (PRD), and Sichuan Basin (SCB), highlighting the
 423 severity of summer O₃ pollution across China.

424 Substantial discrepancies existed between observed and simulated O₃ across all CBC
 425 scenarios. The BASE scenario, in particular, systematically underestimated both mean
 426 and extreme O₃, especially in northern regions (latitude > 30° N). Avg-O3MDA8
 427 underestimations reached -16.1 ppbv in North China and -11.2 ppbv in Northwest
 428 China, with moderate underestimations in East (-5.1 ppbv) and Northeast China (-4.8
 429 ppbv) (Fig. 3; Table S4). Similarly, 90th-O3MDA8 was underestimated by 32.9% in
 430 North China and 26.2% in Northwest China, with smaller NMB (-9.3 to -14.2%)
 431 elsewhere except South China (Table S5). These results indicate that the BASE scenario
 432 poorly represents both average and high O₃ levels, limiting its ability to capture O₃
 433 formation and transport processes during hot seasons.

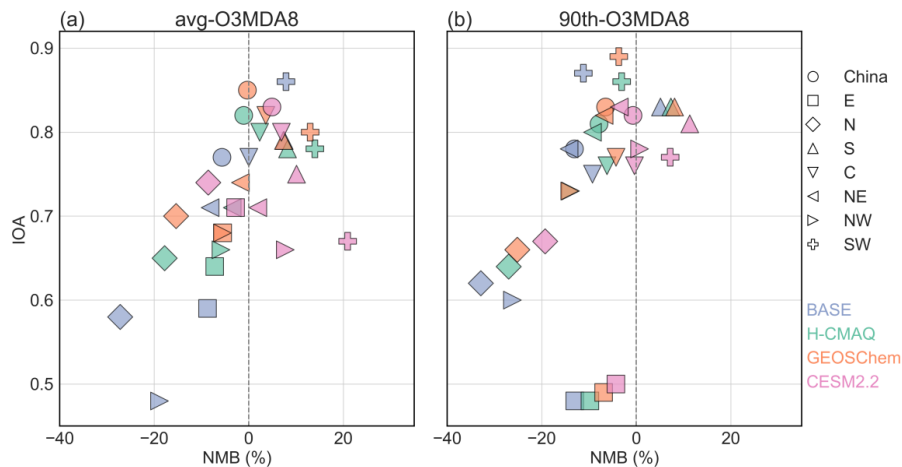
434 By incorporating global model-derived CBCs, significant improvements in both bias
 435 and agreement are observed across China. Based on the NMB values for avg-O3MDA8
 436 and 90th-O3MDA8, the three dynamic CBC scenarios can be ranked as follows: GEOS-
 437 Chem (-0.3%, -6.5%) > H-CMAQ (-1.1%, -7.9%) > CESM2.2 (+4.9%, -0.7%)
 438 (Tables S4-S5). GEOS-Chem consistently yielded the smallest bias, indicating the most
 439 accurate representation of boundary and background O₃ inflow at both average and
 440 extreme levels. Correspondingly, its index of agreement (IOA) reached 0.85 for avg-
 441 O3MDA8 and 0.83 for 90th-O3MDA8, the highest among all scenarios, suggesting
 442 excellent spatial and temporal consistency with observations. The H-CMAQ scenario
 443 also improved upon the BASE case, albeit to a slightly lesser extent, reducing O₃
 444 underestimation while maintaining IOAs of 0.82 (avg-O3MDA8) and 0.81 (90th-
 445 O3MDA8). In contrast, the CESM2.2 scenario exhibited a positive NMB for avg-
 446 O3MDA8 (+4.9%), suggesting a slight overestimation in background inflow. However,
 447 CESM2.2 substantially improved the simulation of O₃ extremes, with a much smaller
 448 NMB (-0.7%) for 90th-O3MDA8 and a still-high IOA of 0.83, highlighting its strength
 449 in reproducing high-O₃ pollution events, especially in regions influenced by complex
 450 terrain and strong photochemistry. Overall, these results demonstrate that applying



451 dynamic CBCs derived from global chemical transport models substantially enhances
 452 the simulation of both average and extreme O₃ concentrations.



453
 454 **Figure 3.** Spatial distribution of avg-O3MDA8 and 90th-O3MDA8 from observations (OBS) and four
 455 CBC scenario simulations. Panels (a, f) show observed avg-O3MDA8 and 90th-O3MDA8 at 1,480
 456 monitoring sites, while panels (b–e, g–j) present site-level normalized mean bias (NMB) for BASE, H-
 457 CMAQ, GEOS-Chem, and CESM2.2 simulations, respectively.



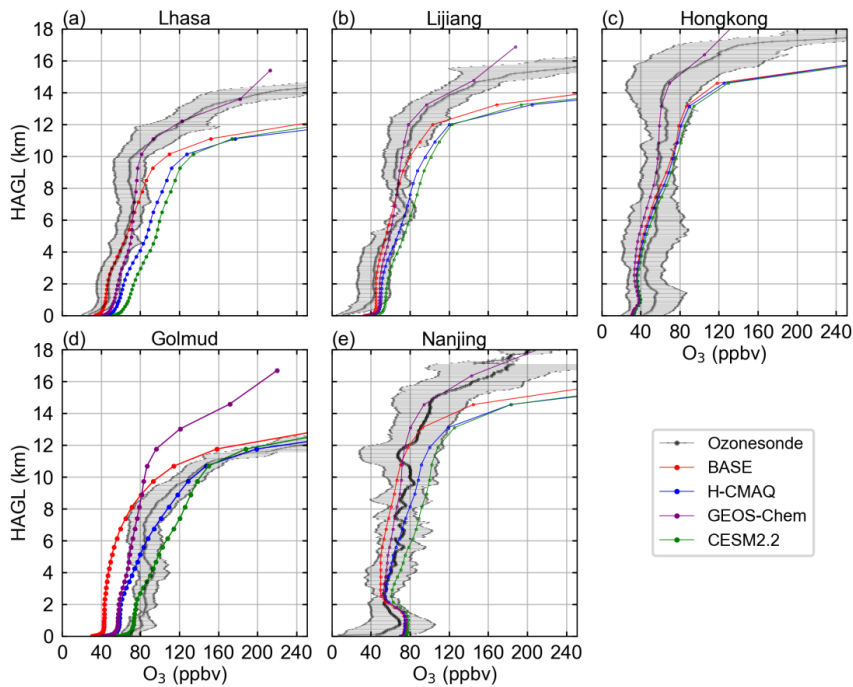
458
 459 **Figure 4.** Comparison of model performance among four CBC scenarios (BASE, H-CMAQ, GEOS-
 460 Chem, and CESM2.2) in terms of Normalized Mean Bias (NMB, %) and Index of Agreement (IOA) for
 461 (a) average daily maximum 8-hour O₃ concentrations (avg-O3MDA8) and (b) the 90th percentile of daily
 462 maximum 8-hour O₃ (90th-O3MDA8) in China and its seven subregions (South (S), East (E), North (N),
 463 Central (C), Northeast (NE), Northwest (NW), and Southwest (SW)).

464 At the regional scale, however, differences among the three dynamic CBC scenarios
 465 become regionally differentiated (Fig. 4). Although GEOS-Chem and H-CMAQ
 466 consistently show the best nationwide performance, CESM2.2 demonstrates superior
 467 accuracy in several regions. For instance, CESM2.2 achieves the smallest NMB and
 468 highest IOA in the north (N), northeast (NE), east (E) and northwest (NW) regions for
 469 both avg-O3MDA8 and 90th-O3MDA8, reflecting its strength in capturing high O₃



470 events in areas. In the SW region, CESM2.2 outperforms other models with a positive
471 NMB yet high IOA, indicating a well-aligned simulation of elevated background O_3
472 levels. In contrast, GEOS-Chem exhibits balanced performance across most regions,
473 notably achieving relatively low NMB and high IOA in the east (E), central (C), and
474 northeastern (NE) regions. These areas are typically influenced by continental outflow
475 and moderate photochemistry, conditions under which GEOS-Chem's background O_3
476 input appears to be well-optimized. H-CMAQ offers moderate improvement relative to
477 the BASE scenario across most regions, with less extreme biases than BASE and
478 slightly lower IOA compared to CESM2.2 or GEOS-Chem.

479 **3.2.3 Vertical O_3 profile Evaluation**



480
481 **Figure 5.** Comparison of vertical O_3 profiles between four CBC scenario simulation (BASE, H-CMAQ,
482 GEOS-Chem, and CESM2.2) and sounding observations at five stations across China.
483
484



485 **Table 3** Comparison and evaluation of vertical O₃ concentration profiles (ppbv) at each sounding
486 station.

	Lhasa	Lijiang	Hongkong	Golmud	Nanjing
Lower troposphere (0-3 km)					
OBS	45.4	39.1	49.9	64.9	57.9
BASE	45.3	45.1	40.8	43.0	64.8
H-CMAQ	60.6	50.6	41.3	59.4	67.0
GEOS-Chem	54.8	48.8	39.5	57.5	67.3
CESM2.2	70.4	55.7	41.9	74.6	71.0
Mid-to-upper troposphere (3-10 km)					
OBS	66.7	62.1	53.9	85.0	68.2
BASE	75.1	62.0	51.4	62.7	56.1
H-CMAQ	94.9	74.8	53.9	94.7	71.5
GEOS-Chem	72.6	62.9	45.8	73.8	62.2
CESM2.2	104.0	81.4	56.7	112.0	83.5
lower stratosphere (10-16 km)					
OBS	230.8	122.1	68.1	174.6	92.3
BASE	306.6	211.7	106.5	288.1	117.7
H-CMAQ	394.4	259.3	112.8	367.7	149.7
GEOS-Chem	147.5	106.6	66.8	131.8	85.7
CESM2.2	371.3	249.3	116.0	332.6	153.8

487 To assess the performance of the model in simulating vertical O₃ distribution under
488 different Chemical Boundary Conditions (CBCs), we compared the simulated O₃
489 profiles from the four scenarios with observational data from five ozonesonde stations
490 (Fig. 5). To better evaluate model performance at different altitudes, we computed mean
491 O₃ concentrations within three representative vertical layers: the lower troposphere (0–
492 3 km), the middle-to-upper troposphere (3–10 km), and the lower stratosphere (10–16
493 km), as summarized in Table 3.

494 In lower troposphere (0–3km), observed O₃ concentrations in this layer ranged from
495 ~39 to 65 ppbv across the five sites. O₃ concentrations in the lower troposphere are
496 sensitive to both local emissions and background inflow. The BASE scenario generally
497 underestimated O₃, whereas incorporating dynamic CBCs increased near-surface
498 concentrations. Among the scenarios, GEOS-Chem exhibited the most balanced
499 performance, with mean biases typically within ± 10 ppbv. CESM2.2 overestimated O₃
500 substantially at high-altitude sites, e.g., +25.0 ppbv at Lhasa and +9.7 ppbv at Golmud,
501 indicating excessive inflow of near-surface O₃. H-CMAQ also slightly overestimated
502 O₃, but with smaller magnitudes. These results indicate that while dynamic CBCs
503 improve near-surface O₃ representation, overestimation in clean or elevated regions
504 (e.g., Lhasa) must be carefully considered, especially when using CESM2.2.

505 The mid-to-upper troposphere (3~10km) reflects regional background transport, deep
506 convection, and vertical mixing. Observed O₃ levels typically increased with altitude,
507 ranging from ~54 to 85 ppbv. The BASE scenario consistently underestimated O₃ in
508 this layer, particularly in Golmud (~22.3 ppbv) and Nanjing (~12.1 ppbv), due to



509 insufficient O₃ inflow. Dynamic CBCs significantly reduced this bias. H-CMAQ and
510 CESM2.2 both improved model–observation agreement, but CESM2.2 often
511 overestimated O₃ (e.g., +37.3 ppbv in Lhasa), potentially reflecting overly strong
512 entrainment of free-tropospheric O₃. GEOS-Chem again performed best overall,
513 producing values close to observations in Lijiang, Nanjing, and Lhasa, demonstrating
514 a good balance between under- and overestimation. This suggests that GEOS-Chem
515 CBCs offer the most realistic representation of free-tropospheric O₃, while CESM2.2
516 may be too aggressive in polluted or convective regions.

517 In the lower stratosphere (10–16 km), O₃ levels increased sharply in this layer, with
518 observed values ranging from ~68 to 231 ppbv. The BASE scenario significantly
519 overestimated stratospheric O₃ at all sites, especially in Golmud and Lhasa, indicating
520 excessive intrusion of stratospheric O₃ in default boundary inputs. This bias was further
521 amplified in H-CMAQ and CESM2.2, with overestimations exceeding ~164 ppbv and
522 ~140 ppbv in Lhasa and ~193 ppbv and ~158 ppbv in Golmud. From the vertical O₃
523 profile comparison, the elevated biases in the lower stratosphere of BASE, H-CMAQ,
524 and CESM2.2 scenarios may enhance the stratosphere–troposphere exchange (STE),
525 especially in southwestern and southern China, which is significantly influenced by the
526 Qinghai-Tibet Plateau (Fig. 5a-c,e). In contrast, GEOS-Chem was the only CBC that
527 consistently reduced this overestimation, bringing modeled values closer to
528 observations at all sites. For example, it lowered the stratospheric bias in Golmud from
529 +113.5 ppbv (BASE) to -42.8 ppbv and achieved near-perfect agreement in Hong Kong
530 (-1.3 ppbv). Overall, the vertical profile analysis underscore that GEOS-Chem provides
531 the most accurate representation of upper tropospheric and stratospheric O₃ inflow,
532 especially important for western China where STE processes are more active.

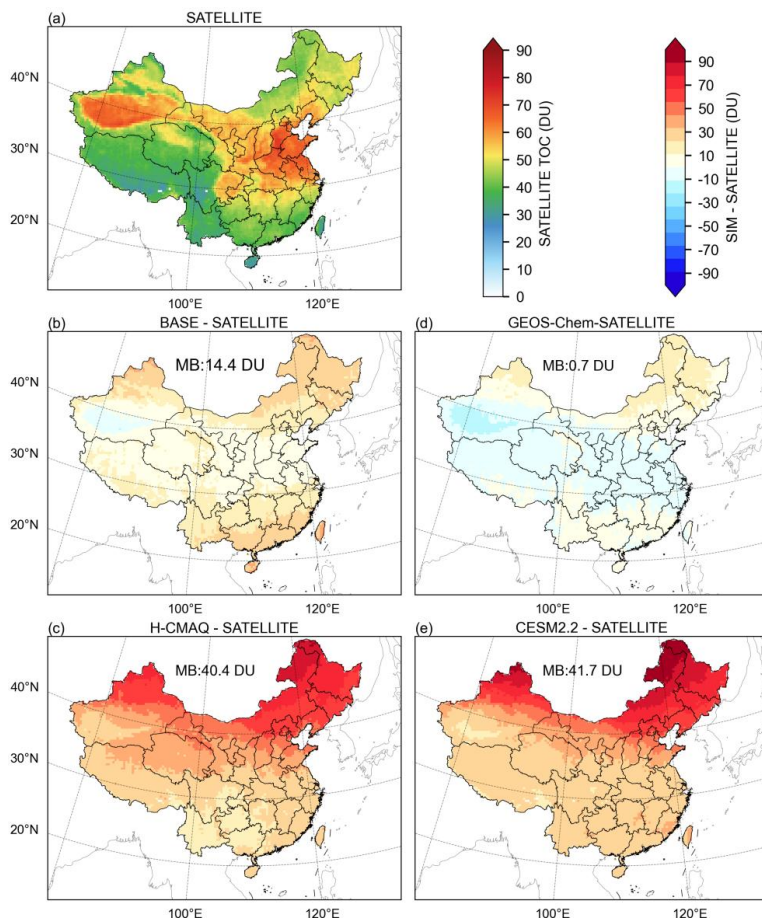
533 **3.2.4 Satellite-Based O₃ Column Assessment**

534 The spatial distribution of tropospheric ozone column (TOC) concentrations provides
535 valuable insights into regional O₃ pollution patterns. In this study, TOC concentrations
536 retrieved from the Environmental Trace Gases Monitoring Instrument (EMI) aboard the
537 Gaofen-5 satellite during July–August 2019 were compared with simulation (SIM)
538 results from four different scenario models (Fig. 6). Observational data from EMI
539 indicate a general increase in TOC concentrations with latitude across China, consistent
540 with previous studies (Zhu et al., 2022; Liu et al., 2022). North China exhibits the
541 highest TOC values among the eastern regions, corresponding to areas known for severe
542 surface-level O₃ pollution (Lu et al., 2018).

543 From the numerical modeling perspective, the simulation scenarios based on the BASE,
544 H-CMAQ, and CESM2.2 models predominantly reflect an overestimation of TOC
545 concentrations. Among them, the BASE scenario demonstrates the least degree of
546 overestimation, particularly in the South China and Northeast China regions, where
547 overestimations range from 20 to 30 DU, while other regions exhibit overestimations
548 between 10 and 20 DU. Both the H-CMAQ and CESM2.2 models show robust
549 overestimations exceeding 20 DU, especially in northern China (north of 35°N), where
550 the overestimation can surpass 40 DU, with the Northeast region registering the highest
551 overestimation, reaching beyond ~50—60 DU. In contrast, the CBCs boundary
552 conditions provided by the GEOS-Chem model yield superior results in simulating the



553 spatial distribution of TOC, with slight overestimations noted in South China and areas
554 north of 40°N, while underestimating concentrations within the latitude range of 30°N
555 to 40°N. The regional mean bias (MB) of model-simulated TOC versus satellite
556 observations was calculated for the mainland of China. The MB of model-simulated
557 TOC (DU) for the four scenarios—BASE, H-CMAQ, CESM2.2, and GEOS-Chem—
558 were 14.4 DU, 40.4 DU, 41.7 DU, and 0.7 DU, respectively, consistent with the analysis
559 results shown in Fig. 5. And the simulation discrepancies for TOC across China are
560 confined to approximately ± 10 DU, indicating that GEOS-Chem's CBCs represent the
561 optimal boundary condition input for regional O₃ modeling in China area.



562

563 **Figure 6.** Comparison of tropospheric ozone column (TOC) distributions over China between satellite
564 observations and model simulations. Panel (a) shows the TOC retrieved from satellite measurements,
565 while panels (b–e) depict the differences (MB) between simulated TOC from the BASE, H-CMAQ,
566 GEOS-Chem, and CESM2.2 scenarios and the satellite retrieval.

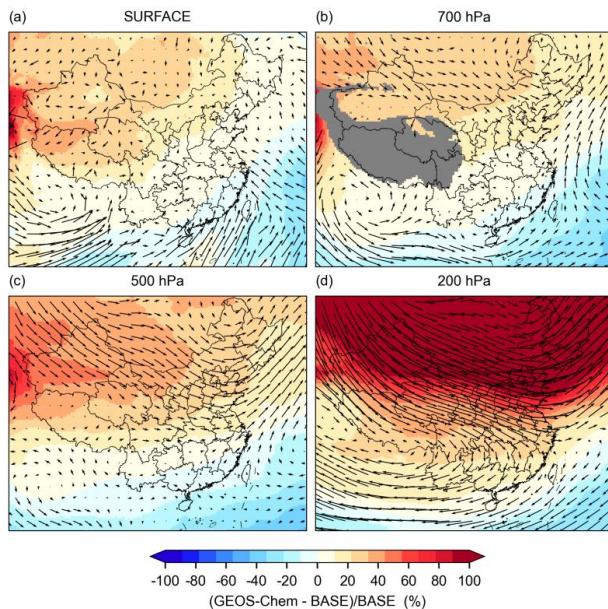
567



568 **3.3 Mechanism of the impact of CBCs on O₃ formation**

569 **3.3.1 General impact of synoptic-scale circulation**

570 CBCs regulate regional O₃ by controlling the inflow of background O₃ and precursors
571 at model boundaries. Given the superior performance of GEOS-Chem in reproducing
572 surface and vertical O₃ based on our validations, we further contrast GEOS-Chem with
573 the BASE scenario to highlight the role of CBCs in cross-boundary transport at the
574 surface and at 700, 500, and 200 hPa isobaric surfaces (Fig. 7).



575
576 **Figure 7.** Normalized mean bias (NMB, (GEOS-Chem – BASE)/BASE) of mean O₃ concentrations and
577 corresponding mean flow fields at surface and 700, 500, and 200 hPa isobaric surfaces over the
578 simulation domain. (The grey area indicates invalid value.)

579 In southeastern China, summer monsoonal flow carried relatively clean marine air into
580 the mid-lower troposphere, lowering background O₃ and suppressing accumulation
581 over eastern and southern regions, where GEOS-Chem boundary conditions produced
582 slightly reduced concentrations (<4%, Fig. 7a-7b). This dilution effect is consistent with
583 the characteristic influence of the Western Pacific Subtropical High during summer,
584 which effectively flushes the coastal boundary layer with cleaner oceanic air masses. In
585 contrast, along the northern and western boundaries, GEOS-Chem introduced
586 substantially higher O₃ than BASE. Adverted by prevailing northwesterlies, these
587 inflows penetrated deep into inland China, increasing surface O₃ by more than 10%
588 across most regions and by over 20% in northern and northwestern China. The
589 magnitude of this enhancement aligns with the recognized impact of long-range
590 transport from Eurasia, which often elevates the ozone baseline in northern China. The
591 influence of CBC was even stronger at higher altitudes (Fig. 7c-7d). At 500 and 200
592 hPa, GEOS-Chem introduced markedly higher O₃ than BASE, reflecting enhanced

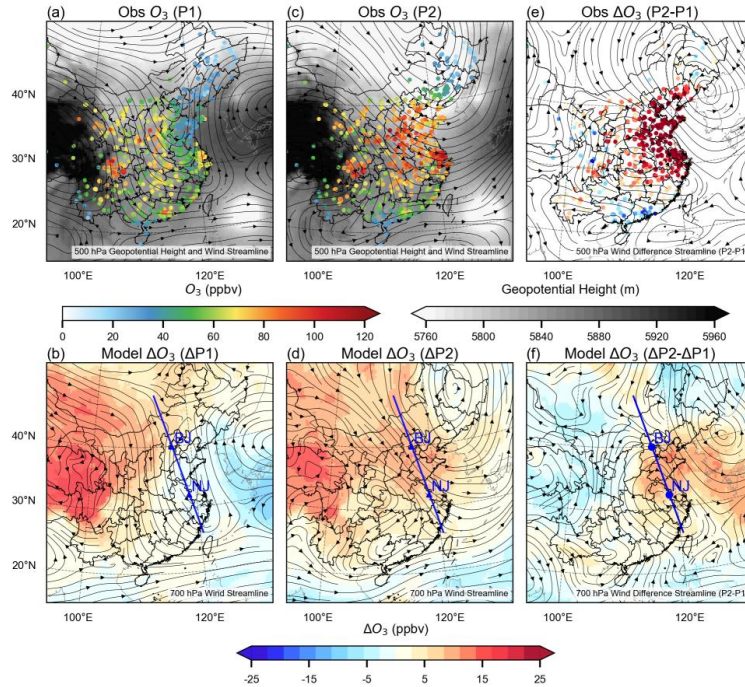


593 background inflows and contributions from stratospheric air masses. This vertical
594 gradient in CBC sensitivity underscores the role of the free troposphere as a reservoir
595 for long-lived O₃. Such upper-level enhancements have important surface implications,
596 as downward mixing and stratosphere–troposphere exchange (STE) can transport high-
597 O₃ air into the boundary layer under favorable meteorological conditions, especially
598 during the passage of cold fronts or deep convective mixing, further exacerbating
599 pollution episodes.

600 Overall, these results highlight that the mechanistic impact of CBC on O₃ formation
601 arises from a synergistic combination of boundary inflow composition and large-scale
602 circulation. While oceanic inflows tend to dilute O₃ in southern and eastern regions,
603 strong continental and stratospheric inflows from the north and west can significantly
604 elevate both free-tropospheric and surface O₃, amplifying pollution severity in inland
605 China. These findings confirm that accurate CBCs are not merely a model constraint
606 but a vital component for capturing the dynamic interplay between local
607 photochemistry and global atmospheric circulation.

608 **3.3.2 Case Study: Synoptic-Scale Circulation Dynamics Modulating CBC
609 Impacts**

610 The influence of CBC varies dynamically with large-scale meteorological conditions
611 rather than remaining static. During summer, synoptic disturbances such as the Western
612 Pacific Subtropical High extensions, tropical cyclone activity, and East Asian westerly
613 jet fluctuations reshape regional circulation patterns and modulate the transport of
614 polluted or clean air masses into the model domain. These circulation changes,
615 characterized by alternating cyclonic and anticyclonic flows, substantially alter the
616 efficiency of transboundary transport and consequently affect CBC impacts on near-
617 surface O₃ simulations. Here, we examined two sequential circulation regimes during
618 August 2019 associated with successive typhoon events: Super Typhoon Lekima and
619 Typhoon Krosa. These events created distinctly different transport patterns that
620 modulated how boundary conditions influenced surface O₃ across China. Based on this
621 evolution, we define two phases: Phase 1 (P1, 10–14 August, during Lekima's landfall
622 and decay in Eastern China) and Phase 2 (P2, 15–19 August, controlled by post-trough
623 northwesterlies) (Fig. 8).



624

625 **Figure 8.** (a) Distribution of 500 hPa winds (streamlines), geopotential height (contours), and surface O_3
626 observations (dots) during P1; (b) Distribution of 700 hPa winds (streamlines), and difference in modeled
627 surface O_3 between GEOS-Chem CBC and BASE during P1; (c) same as (a) but for P2; (d) same as (b)
628 but for P2; (e) differences in observed surface O_3 and 500 hPa winds between P1 and P2; (f) differences
629 in simulated surface O_3 and 700 hPa winds between P1 and P2. Blue lines indicate the locations of vertical
630 cross-sectional analyses, extending from north to south through Beijing (BJ) and Nanjing (NJ).

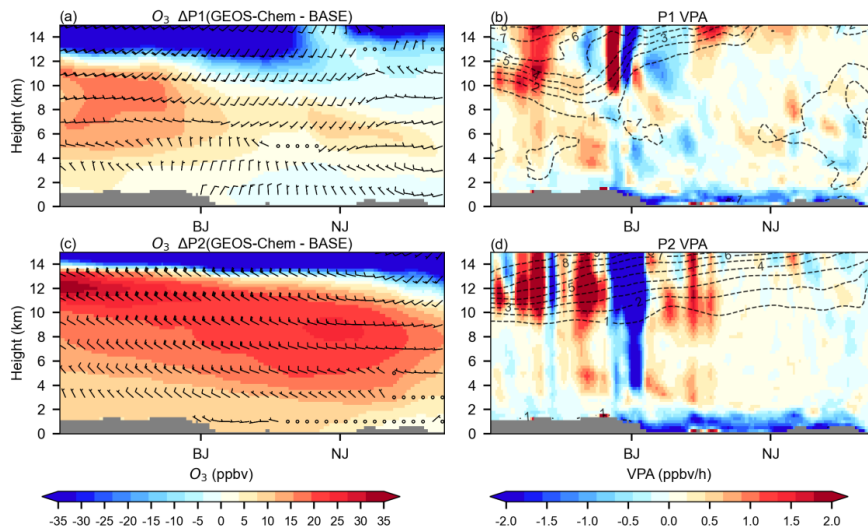
631 P1 occurred during the landfall and decay of Super Typhoon Lekima over the Yangtze
632 River Delta (Fig 8a and 8b, and Fig. S2). The tropospheric circulation was dominated
633 by a deep trough linked to the typhoon's remnant system, which enhanced southeasterly
634 flow of marine air into eastern China. This pattern promoted deep convection and
635 vigorous vertical mixing, leading to a pronounced coastal-inland gradient in surface O_3 :
636 marine-influenced coastal areas exhibited low concentrations (<50 ppbv), while inland
637 regions maintained moderate-to-high levels (60–90 ppbv). The cyclonic circulation
638 disrupted typical westerly transport pathways, reducing transboundary O_3 influence
639 from northern and western source regions. Consequently, the BASE scenario
640 overestimated O_3 by 15–25 ppbv over oceanic regions where static boundary conditions
641 failed to capture typhoon-enhanced marine influence, while underestimating
642 concentrations by 10–20 ppbv in northwestern China where continental transport
643 remained active but was inadequately represented by the Pacific-based boundary profile
(Fig. 8b).

645 By contrast, P2 was characterized by a dominant northwesterly flow across central and
646 eastern China, situated behind a mid-level trough, while a high-pressure system
647 strengthened over western China (Fig. 8c-8d). This "east-trough, west-ridge"
648 configuration facilitated the efficient advection of O_3 -rich air from western and northern



649 source regions, resulting in the noticeable O_3 elevations observed across the region (Fig.
650 8c-d). Model sensitivity analysis confirms that accurately representing these high- O_3
651 boundary inflows under such transport-favorable conditions elevates surface
652 concentrations by 10–15 ppbv in the most affected areas (Fig. 8d). These results
653 demonstrate that the BASE scenario, employing static boundary conditions,
654 systematically underestimates cross-boundary pollution contributions during
655 dynamically active periods when long-range transport is of importance.
656 The difference between P2 and P1 (Fig. 8e–f) illustrates a marked meteorological
657 transition from a pollution-scavenging cyclonic regime during P1 to a pollution-
658 accumulating regime in P2, characterized by trough-driven northwesterly transport and
659 high-pressure-induced stability. This synoptic shift corresponded with observed surface
660 O_3 increases of 30–60 ppbv across northern and central-eastern China. These regions
661 aligned spatially with the anticyclonic circulation, where enhanced subsidence favored
662 the accumulation of transported O_3 . By incorporating chemically realistic CBCs, the
663 simulation attributes approximately 10 ppbv of this O_3 increase to cross-boundary
664 transport during P2 (Fig. 8f), highlighting the essential role of CBCs in accurately
665 capturing O_3 buildup under transport-favorable synoptic regimes.

666
667
668
669



670
671 **Figure 9.** (a) Vertical cross-sectional analysis of the O_3 difference between GEOS-Chem CBC and the
672 BASE scenario during P1, the wind bar denotes vertical wind field; (b) vertical distribution of potential
673 vorticity (PV, dashed contours) and vertical transport (VPA, calculated by CMAQ process analysis as the
674 sum of vertical diffusion and vertical advection) during P1; (c) same as (a) but for P2. (d) same as (b) but
675 for P2. The x-axis labels BJ and NJ indicate the locations of Beijing and Nanjing, respectively.

676 To further clarify the role of dynamic CBC in O_3 simulations, we performed vertical
677 cross-sectional analyses using the CMAQ process analysis module along the major



678 transport pathways during P1 and P2 (Fig. 9). Both phases consistently revealed strong
679 cross-boundary transport, with upstream inflows from outside the domain substantially
680 influencing downstream O₃ levels across mainland China. During P1, Typhoon Lekima
681 disrupted the transport corridor near the Yangtze River Delta (approximately 0–4 km),
682 restricting cross-boundary influences mainly to northern inflows affecting the North
683 China Plain (Fig. 9a). In contrast, under post-trough northwesterly flow during P2,
684 cross-boundary transport extended southward from the northern boundary, reaching as
685 far as the Yangtze River Delta (Fig. 9b). The difference between P1 and P2 highlights
686 a distinct transport corridor extending from higher to lower latitudes and from the mid-
687 upper troposphere toward the surface (Fig. S3), further emphasizing the crucial role of
688 dynamic CBCs in shaping O₃ distributions.

689 Here, we demonstrate that cross-boundary transport also occurs in the vertical
690 dimension, with O₃-rich air descending from the upper to the lower troposphere, while
691 stratosphere–troposphere exchange (STE) provided an additional pathway for
692 transboundary inflow. To identify possible STE occurrences, potential vorticity (PV)
693 between 10 and 14 km (above sea level) was examined, adopting a threshold of 2 PVU
694 (PV units, 1 PVU = 10⁻⁶ m² s⁻¹ kg⁻²) to distinguish stratospheric from tropospheric air
695 masses. STE events were evident over northern China during both P1 and P2 (Fig. 9c-
696 d and Fig. S4). In addition, the CMAQ process analyses with GEOS-Chem CBCs
697 corroborated intensified vertical transport between 10 and 14 km in both phases, with
698 distinctly positive contributions from vertical advection and turbulent diffusion. As a
699 result, the joint impact of large-scale advection and vertical mixing processes enabled
700 high-altitude O₃ to intrude into the lower troposphere and ultimately affect downstream
701 regions, even in YRD (such as Nanjing city).

702 **4. Conclusion**

703 This research demonstrates that CBCs represent a critical but often underappreciated
704 component of regional air quality modeling systems. We systematically evaluated the
705 influence of CBCs on regional O₃ simulations over China using the WRF-CMAQ
706 model. Four CBC scenarios were compared: a static BASE scenario using
707 climatological profiles and three dynamic scenarios derived from global chemical
708 transport models (H-CMAQ, GEOS-Chem, and CESM2.2). Overall, dynamic CBCs
709 substantially improved the representation of surface O₃ compared to the static BASE
710 scenario, with GEOS-Chem CBCs performing best. Across China, the normalized mean
711 bias (NMB) for avg-O3MDA8 was reduced from -5.7% (BASE) to -0.3% (GEOS-
712 Chem), and the index of agreement (IOA) increased from 0.77 to 0.85, while the 90th-
713 O3MDA8 percentile NMB improved from -13.1% to -6.5%, and the IOA increased
714 from 0.66 to 0.77. Based on ozonesonde profiles and satellite TOC evaluations, elevated
715 biases were identified in the lower stratosphere for BASE, H-CMAQ, and CESM2.2,
716 which may lead to overestimation of background O₃ concentrations, particularly during
717 STE events.

718 The influence of CBCs varies dynamically with large-scale meteorological conditions
719 rather than remaining static. During summer, synoptic disturbances such as the Western



720 Pacific Subtropical High extensions, tropical cyclone activity, and East Asian westerly
721 jet fluctuations reshape regional circulation patterns and modulate the transport of
722 polluted or clean air masses into the model domain. These circulation changes,
723 characterized by alternating cyclonic and anticyclonic flows, substantially alter the
724 efficiency of transboundary transport and consequently affect CBC impacts on near-
725 surface O₃ simulations. Generally, oceanic inflows from the south dilute O₃ in
726 southeastern and coastal areas, whereas strong continental and stratospheric inflows
727 from northern and western boundaries significantly modulate tropospheric O₃,
728 especially in downwind regions of the synoptic systems.

729 A comparative analysis of two successive synoptic regimes in July - August 2019,
730 which shifted from a cyclone-dominated, pollution-scavenging phase to a post-trough
731 northwesterly flow favorable for accumulation, revealed that dynamic circulation
732 patterns enhanced cross-boundary transport both horizontally (via continental inflows
733 from northern and western boundaries) and vertically (via stratosphere-troposphere
734 exchange). The combined effects of these transport processes increased O₃
735 concentrations by 10–20% during high-pollution events over eastern China. These
736 results underscore that accurate representation of dynamic CBCs is essential to capture
737 circulation-driven horizontal and vertical transport and their integrated impact on
738 regional O₃ distributions.

739 Our findings demonstrate that the choice of CBCs is not merely a technicality but a
740 dynamic determinant of simulated O₃ levels for regional CTM, especially when facing
741 synoptic regimes that favor long-range transport or vertical exchange. This underscores
742 the necessity of moving beyond static boundary conditions in regional air quality
743 modeling. To advance predictive capability, future efforts should pursue multi-model
744 ensembles to quantify CBC uncertainty and explore the integration of real-time global
745 fields into regional CTM forecasting systems. By elucidating the critical interplay
746 between large-scale transport and regional pollution, this study provides a scientific
747 foundation not only for improving O₃ forecasting but also for designing effective
748 transboundary air quality management strategies.

749 **Acknowledgments**

750 This research is supported by the National Key Research and Development Program
751 (grant no. 2023YFC3709301), the National Natural Science Foundation Project (grant
752 no. 42575120 and no. 42293322), the Youth Fund Project of the Sichuan Provincial
753 Natural Science Foundation (24NSFSC2988), the Fundamental Research Funds for the
754 Central Universities (Grant No. YJ202313). We acknowledge use of the hyperspectral
755 remote sensing products of atmospheric compositions developed by Prof. Cheng Liu's
756 group at the University of Science and Technology of China. The authors also thank the
757 Tsinghua University for developing and sharing the MEIC emission inventory.

758 **Financial Support**

759 This research is supported by the National Key Research and Development Program
760 (grant no. 2023YFC3709301), the National Natural Science Foundation Project (grant
761 no. 42575120 and no. 42293322), the Youth Fund Project of the Sichuan Provincial
762 Natural Science Foundation (24NSFSC2988), the Fundamental Research Funds for the
763 Central Universities (Grant No. YJ202313).



764 **Author Contributions**

765 N.W. and F.Y. designed the research. Y.D. conducted the simulation. Y.D. and N.W.
766 wrote the manuscript. S.L., Y.H., B.L. and G.S. contributed to the interpretation of the
767 results. R.H., B.L., Y.J., N.W. and Y.F. provided critical feedback and helped to improve
768 the manuscript.

769 **Competing Interests**

770 The authors declare that they have no known competing financial interests or personal
771 relationships that could have appeared to influence the work.

772 **Data Availability**

773 The numerical simulation results were stored on Shuguang supercomputer, and results
774 can be acquired from Nan Wang (nan.wang@scu.edu.cn)

775 **References**

776 Bai, L., Wang, J., Ma, X., and Lu, H.: Air pollution forecasts: An overview, International journal of
777 environmental research and public health, 15, 780, 2018.
778 Bai Zhixuan, B. J.: Golmud site SWOP atmospheric composition agent open line data (2020 -2021),
779 National Tibetan Plateau Data Center [dataset], 10.11888/Atmos.tpdc.300057, 2022.
780 Bai Zhixuan, B. J.: Lijiang SWOP atmospheric composition comprehensive sounding data set
781 (2021-2022), National Tibetan Plateau Data Center [dataset], 10.11888/Atmos.tpdc.300156, 2023.
782 Byun, D. and Schere, K. L.: Review of the governing equations, computational algorithms, and other
783 components of the Models-3 Community Multiscale Air Quality (CMAQ) modeling system,
784 Applied mechanics reviews, 59, 51-77, 2006.
785 Campbell, P. C., Bash, J. O., and Spero, T. L.: Updates to the Noah land surface model in WRF-
786 CMAQ to improve simulated meteorology, air quality, and deposition, Journal of Advances in
787 Modeling Earth Systems, 11, 231-256, 2019.
788 Carter, W. P. and Heo, G.: Development of revised SAPRC aromatics mechanisms, Atmospheric
789 environment, 77, 404-414, 2013.
790 Chiu, Y.-H. M., Wilson, A., Hsu, H.-H. L., Jamal, H., Mathews, N., Kloog, I., Schwartz, J., Bellinger, D.
791 C., Xhani, N., and Wright, R. O.: Prenatal ambient air pollutant mixture exposure and
792 neurodevelopment in urban children in the Northeastern United States, Environmental research,
793 233, 116394, 2023.
794 Dou, X., Yu, S., Li, J., Sun, Y., Song, Z., Yao, N., and Li, P.: The WRF-CMAQ Simulation of a Complex
795 Pollution Episode with High-Level O₃ and PM_{2.5} over the North China Plain: Pollution
796 Characteristics and Causes, Atmosphere, 15, 198, 2024.
797 Eastham, S. D., Weisenstein, D. K., and Barrett, S. R.: Development and evaluation of the unified
798 tropospheric-stratospheric chemistry extension (UCX) for the global chemistry-transport model
799 GEOS-Chem, Atmospheric Environment, 89, 52-63, 2014.
800 Foley, K. M., Pouliot, G. A., Eyth, A., Aldridge, M. F., Allen, C., Appel, K. W., Bash, J. O., Beardsley, M.,
801 Beidler, J., and Choi, D.: 2002–2017 anthropogenic emissions data for air quality modeling over
802 the United States, Data in Brief, 47, 109022, 2023.
803 Gao, C., Zhang, X., Xiu, A., Tong, Q., Zhao, H., Zhang, S., Yang, G., Zhang, M., and Xie, S.:



804 Intercomparison of multiple two-way coupled meteorology and air quality models (WRF v4. 1.1–
805 CMAQ v5. 3.1, WRF–Chem v4. 1.1, and WRF v3. 7.1–CHIMERE v2020r1) in eastern China,
806 geoscientific model development, 17, 2471–2492, 2024.

807 Geng, G., Liu, Y., Liu, Y., Liu, S., Cheng, J., Yan, L., Wu, N., Hu, H., Tong, D., and Zheng, B.: Efficacy
808 of China's clean air actions to tackle PM_{2.5} pollution between 2013 and 2020, *Nature Geoscience*,
809 17, 987–994, 2024.

810 Godowitch, J. M., Gilliam, R. C., and Roselle, S. J.: Investigating the impact on modeled ozone
811 concentrations using meteorological fields from WRF with an updated four-dimensional data
812 assimilation approach, *Atmospheric Pollution Research*, 6, 305–311, 2015.

813 Goldberg, D. L., Vinciguerra, T. P., Hosley, K. M., Loughner, C. P., Carty, T. P., Salawitch, R. J., and
814 Dickerson, R. R.: Evidence for an increase in the ozone photochemical lifetime in the eastern United
815 States using a regional air quality model, *Journal of Geophysical Research: Atmospheres*, 120,
816 12778–12793, 2015.

817 Grell, G. A., Peckham, S. E., Schmitz, R., McKeen, S. A., Frost, G., Skamarock, W. C., and Eder, B.:
818 Fully coupled "online" chemistry within the WRF model, *Atmospheric environment*, 39, 6957–6975,
819 2005.

820 Hersbach, H., Bell, B., Berrisford, P., Biavati, G., Horányi, A., Muñoz Sabater, J., Nicolas, J., Peubey,
821 C., Radu, R., and Rozum, I.: ERA5 hourly data on pressure levels from 1940 to present, Copernicus
822 climate change service (c3s) climate data store (cds), 10, 24381, 2023.

823 Hogrefe, C., Liu, P., Pouliot, G., Mathur, R., Roselle, S., Flemming, J., Lin, M., and Park, R. J.: Impacts
824 of different characterizations of large-scale background on simulated regional-scale ozone over
825 the continental United States, *Atmospheric Chemistry and Physics*, 18, 3839–3864, 2018.

826 Hu, J., Chen, J., Ying, Q., and Zhang, H.: One-year simulation of ozone and particulate matter in
827 China using WRF/CMAQ modeling system, *Atmospheric Chemistry and Physics*, 16, 10333–10350,
828 2016.

829 Jacob, D. J.: The oxidizing power of the atmosphere, *Handbook of weather, climate and water*, 29–
830 46, 2003.

831 Jerrett, M., Arain, A., Kanaroglou, P., Beckerman, B., Potoglou, D., Sahsuvaroglu, T., Morrison, J.,
832 and Giovis, C.: A review and evaluation of intraurban air pollution exposure models, *Journal of
833 Exposure Science & Environmental Epidemiology*, 15, 185–204, 2005.

834 Lei, Y., Wu, K., Zhang, X., Kang, P., Du, Y., Yang, F., Fan, J., and Hou, J.: Role of meteorology-driven
835 regional transport on O₃ pollution over the Chengdu Plain, southwestern China, *Atmospheric
836 Research*, 285, 10.1016/j.atmosres.2023.106619, 2023.

837 Li, M., Liu, H., Geng, G., Hong, C., Liu, F., Song, Y., Tong, D., Zheng, B., Cui, H., and Man, H.:
838 Anthropogenic emission inventories in China: a review, *National Science Review*, 4, 834–866, 2017a.

839 Li, M., Zhang, Q., Kurokawa, J.-i., Woo, J.-H., He, K., Lu, Z., Ohara, T., Song, Y., Streets, D. G., and
840 Carmichael, G. R.: MIX: a mosaic Asian anthropogenic emission inventory under the international
841 collaboration framework of the MICS-Asia and HTAP, *Atmospheric Chemistry and Physics*, 17,
842 935–963, 2017b.

843 Liu, J., Strode, S. A., Liang, Q., Oman, L. D., Colarco, P. R., Fleming, E. L., Manyin, M. E., Douglass, A.
844 R., Ziemke, J. R., and Lamsal, L. N.: Change in tropospheric ozone in the recent decades and its
845 contribution to global total ozone, *Journal of Geophysical Research: Atmospheres*, 127,
846 e2022JD037170, 2022.

847 Lu, X., Zhang, L., Wang, X., Gao, M., Li, K., Zhang, Y., Yue, X., and Zhang, Y.: Rapid increases in



848 warm-season surface ozone and resulting health impact in China since 2013, Environmental
849 Science & Technology Letters, 7, 240-247, 2020.

850 Lu, X., Hong, J., Zhang, L., Cooper, O. R., Schultz, M. G., Xu, X., Wang, T., Gao, M., Zhao, Y., and
851 Zhang, Y.: Severe surface ozone pollution in China: a global perspective, Environmental Science &
852 Technology Letters, 5, 487-494, 2018.

853 Mallard, M. S., Spero, T. L., and Taylor, S. M.: Examining WRF's sensitivity to contemporary land-
854 use datasets across the contiguous United States Using Dynamical Downscaling, Journal of applied
855 meteorology and climatology, 57, 2561-2583, 2018.

856 Malley, C. S., Henze, D. K., Kuylenstierna, J. C., Vallack, H. W., Davila, Y., Anenberg, S. C., Turner, M.
857 C., and Ashmore, M. R.: Updated global estimates of respiratory mortality in adults \geq 30 years of
858 age attributable to long-term ozone exposure, Environmental health perspectives, 125, 087021,
859 2017.

860 Mao, J., Fan, S., Jacob, D. J., and Travis, K. R.: Radical loss in the atmosphere from Cu-Fe redox
861 coupling in aerosols, Atmospheric Chemistry and Physics, 13, 509-519, 2013.

862 Mao, J., Li, L., Li, J., Sulaymon, I. D., Xiong, K., Wang, K., Zhu, J., Chen, G., Ye, F., and Zhang, N.:
863 Evaluation of long-term modeling fine particulate matter and ozone in China during 2013–2019,
864 Frontiers in Environmental Science, 10, 872249, 2022a.

865 Mao, M., Rao, L., Jiang, H., He, S., and Zhang, X.: Air pollutants in metropolises of eastern coastal
866 China, International Journal of Environmental Research and Public Health, 19, 15332, 2022b.

867 Monks, P. S., Archibald, A., Colette, A., Cooper, O., Coyle, M., Derwent, R., Fowler, D., Granier, C.,
868 Law, K. S., and Mills, G.: Tropospheric ozone and its precursors from the urban to the global scale
869 from air quality to short-lived climate forcer, Atmospheric chemistry and physics, 15, 8889-8973,
870 2015.

871 Ni, R., Lin, J., Yan, Y., and Lin, W.: Foreign and domestic contributions to springtime ozone over
872 China, Atmospheric Chemistry and Physics, 18, 11447-11469, 2018.

873 Park, R. J., Jacob, D. J., Field, B. D., Yantosca, R. M., and Chin, M.: Natural and transboundary
874 pollution influences on sulfate-nitrate-ammonium aerosols in the United States: Implications for
875 policy, Journal of Geophysical Research: Atmospheres, 109, 2004.

876 Parrella, J., Jacob, D., Liang, Q., Zhang, Y., Mickley, L., Miller, B., Evans, M., Yang, X., Pyle, J., and
877 Theys, N.: Tropospheric bromine chemistry: implications for present and pre-industrial ozone and
878 mercury, Atmospheric Chemistry and Physics, 12, 6723-6740, 2012.

879 Sahu, S. K., Liu, S., Liu, S., Ding, D., and Xing, J.: Ozone pollution in China: Background and
880 transboundary contributions to ozone concentration & related health effects across the country,
881 Science of the Total Environment, 761, 144131, 2021.

882 Shen, C., Shen, A., Cui, Y., Chen, X., Liu, Y., Fan, Q., Chan, P., Tian, C., Wang, C., and Lan, J.:
883 Spatializing the roughness length of heterogeneous urban underlying surfaces to improve the
884 WRF simulation-part 1: A review of morphological methods and model evaluation, Atmospheric
885 Environment, 270, 118874, 2022.

886 Shen, Y., Liu, J., Chen, Z., Yang, M., Shu, L., Gai, C., and Jiang, Y.: Influence of wind flows on surface
887 O3 variation over a Coastal Province in Southeast China, Atmosphere, 15, 262, 2024.

888 Siewert, J. and Kroszczynski, K.: Evaluation of high-resolution land cover geographical data for the
889 WRF model simulations, Remote Sensing, 15, 2389, 2023.

890 Solazzo, E., Bianconi, R., Vautard, R., Appel, K. W., Moran, M. D., Hogrefe, C., Bessagnet, B., Brandt,
891 J., Christensen, J. H., Chemel, C., Coll, I., Denier van der Gon, H., Ferreira, J., Forkel, R., Francis, X. V.,



892 Grell, G., Grossi, P., Hansen, A. B., Jeričević, A., Kraljević, L., Miranda, A. I., Nopmongcol, U., Pirovano, G.,
893 Prank, M., Riccio, A., Sartelet, K. N., Schaap, M., Silver, J. D., Sokhi, R. S., Vira, J., Werhahn, J.,
894 Wolke, R., Yarwood, G., Zhang, J., Rao, S. T., and Galmarini, S.: Model evaluation and ensemble
895 modelling of surface-level ozone in Europe and North America in the context of AQMEII,
896 *Atmospheric Environment*, 53, 60–74, <https://doi.org/10.1016/j.atmosenv.2012.01.003>, 2012.
897 Tarasick, D., Galbally, I. E., Cooper, O. R., Schultz, M. G., Ancellet, G., Leblanc, T., Wallington, T. J.,
898 Ziemke, J., Liu, X., and Steinbacher, M.: Tropospheric Ozone Assessment Report: Tropospheric
899 ozone from 1877 to 2016, observed levels, trends and uncertainties, *Elem Sci Anth*, 7, 39, 2019.
900 Wang, K., Tong, Y., Gao, J., Gao, C., Wu, K., Yue, T., Qin, S., and Wang, C.: Impacts of LULC, FDDA,
901 Topo-wind and UCM schemes on WRF-CMAQ over the Beijing-Tianjin-Hebei region, China,
902 *Atmospheric Pollution Research*, 12, 292–304, 2021a.
903 Wang, N., Huang, X., Xu, J., Wang, T., Tan, Z.-m., and Ding, A.: Typhoon-boosted biogenic emission
904 aggravates cross-regional ozone pollution in China, *Science Advances*, 8, eabl6166, 2022.
905 Wang, N., Lyu, X., Deng, X., Huang, X., Jiang, F., and Ding, A.: Aggravating O₃ pollution due to
906 NO_x emission control in eastern China, *Science of the Total Environment*, 677, 732–744, 2019.
907 Wang, N., Du, Y., Chen, D., Meng, H., Chen, X., Zhou, L., Shi, G., Zhan, Y., Feng, M., and Li, W.:
908 Spatial disparities of ozone pollution in the Sichuan Basin spurred by extreme, hot weather,
909 *Atmospheric Chemistry and Physics*, 24, 3029–3042, 2024.
910 Wang, N., Xu, J., Pei, C., Tang, R., Zhou, D., Chen, Y., Li, M., Deng, X., Deng, T., and Huang, X.: Air
911 quality during COVID-19 lockdown in the Yangtze River Delta and the Pearl River Delta: Two
912 different responsive mechanisms to emission reductions in China, *Environmental Science &*
913 *Technology*, 55, 5721–5730, 2021b.
914 Wang, T., Xue, L., Brimblecombe, P., Lam, Y. F., Li, L., and Zhang, L.: Ozone pollution in China: A
915 review of concentrations, meteorological influences, chemical precursors, and effects, *Science of*
916 *the Total Environment*, 575, 1582–1596, 2017.
917 Wang, Y., Logan, J. A., and Jacob, D. J.: Global simulation of tropospheric O₃-NO x-hydrocarbon
918 chemistry: 2. Model evaluation and global ozone budget, *Journal of Geophysical Research: Atmospheres*, 103, 10727–10755, 1998.
919
920 Wang, Y., Gao, W., Wang, S., Song, T., Gong, Z., Ji, D., Wang, L., Liu, Z., Tang, G., and Huo, Y.:
921 Contrasting trends of PM_{2.5} and surface-ozone concentrations in China from 2013 to 2017,
922 *National Science Review*, 7, 1331–1339, 2020.
923 WHO: Ambient air pollution: A global assessment of exposure and burden of disease, *Clean Air*
924 *Journal*, 26, 6–6, 2016.
925 Yahya, K., He, J., and Zhang, Y.: Multiyear applications of WRF/Chem over continental US: Model
926 evaluation, variation trend, and impacts of boundary conditions, *Journal of Geophysical Research: Atmospheres*, 120, 12748–12777, 2015.
927
928 Yarwood, G., Jung, J., Whitten, G. Z., Heo, G., Mellberg, J., and Estes, M.: Updates to the Carbon
929 Bond mechanism for version 6 (CB6), 9th Annual CMAS Conference, Chapel Hill, NC, 11–13,
930 Zhang, J., Wei, Y., and Fang, Z.: Ozone pollution: a major health hazard worldwide, *Frontiers in*
931 *immunology*, 10, 2518, 2019a.
932 Zhang, Q., Zheng, Y., Tong, D., Shao, M., Wang, S., Zhang, Y., Xu, X., Wang, J., He, H., and Liu, W.:
933 Drivers of improved PM_{2.5} air quality in China from 2013 to 2017, *Proceedings of the National*
934 *Academy of Sciences*, 116, 24463–24469, 2019b.
935 Zhao, F., Liu, C., Hu, Q., Xia, C., Zhang, C., and Su, W.: High Spatial Resolution Ozone Profiles



936 Retrieved from the First Chinese Ultraviolet–Visible Hyperspectral Satellite Instrument, Engineering,
937 32, 106–115, 2024.

938 Zheng, B., Cheng, J., Geng, G., Wang, X., Li, M., Shi, Q., Qi, J., Lei, Y., Zhang, Q., and He, K.: Mapping
939 anthropogenic emissions in China at 1 km spatial resolution and its application in air quality
940 modeling, *Science Bulletin*, 66, 612–620, 2021.

941 Zhixuan, B.: Lhasa SWOP atmospheric composition comprehensive sounding data set (2019–2020),
942 National Tibetan Plateau Data Center [dataset], 10.11888/Atmos.tpdc.300007, 2023.

943 Zhu, Q., Bi, J., Liu, X., Li, S., Wang, W., Zhao, Y., and Liu, Y.: Satellite-based long-term
944 spatiotemporal patterns of surface ozone concentrations in China: 2005–2019, *Environmental*
945 *health perspectives*, 130, 027004, 2022.

946 Zhu, Y., Liu, Y., Li, S., Wang, H., Lu, X., Wang, H., Shen, C., Chen, X., Chan, P., Shen, A., Wang, H.,
947 Jin, Y., Xu, Y., Fan, S., and Fan, Q.: Assessment of tropospheric ozone simulations in a regional
948 chemical transport model using GEOS-Chem outputs as chemical boundary conditions, *Sci Total*
949 *Environ*, 906, 167485, 10.1016/j.scitotenv.2023.167485, 2024.

950